

14 June 2013 | \$10

Science

A microscopic image showing a dense population of cells on a yellow background. The cells are mostly dark, with some lighter, more distinct structures scattered throughout. The overall appearance is that of a cell culture or a biological specimen under a microscope.

AAAS

gold nanospheres (Fig. 4C) on top of one of our hBN/Gr/MoS₂/Gr heterostructures, which enhanced the optical field in the active layer and allowed for a 10-fold increase in the photocurrent, (Fig. 4, D and E) [see (27) for further details and other examples of the use of plasmonic nanostructures].

Atomically thin heterostructures of semiconducting TMDC present strong light-matter interactions that can lead to large photon absorption and photocurrent production. We are able to reach an extrinsic quantum efficiency of 30%, due to the localized character of the electronic wave functions in TMDCs that leads to large peaks in the DoS associated with van Hove singularities. The same devices demonstrate transistor behavior with on/off ratios exceeding those in previously reported devices. The use of various TMDCs, as well as their combinations, would allow one to create new transparent and flexible photonic and optoelectronic structures and devices with unique properties that surpass current technologies.

References and Notes

1. K. S. Novoselov *et al.*, *Science* **306**, 666 (2004).
2. A. K. Geim, K. S. Novoselov, *Nat. Mater.* **6**, 183 (2007).
3. A. K. Geim, *Science* **324**, 1530 (2009).
4. A. K. Geim, *Rev. Mod. Phys.* **83**, 851 (2011).
5. K. S. Novoselov, *Rev. Mod. Phys.* **83**, 837 (2011).
6. K. S. Novoselov *et al.*, *Proc. Natl. Acad. Sci. U.S.A.* **102**, 10451 (2005).
7. C. R. Dean *et al.*, *Nat. Nanotechnol.* **5**, 722 (2010).

8. L. A. Ponomarenko *et al.*, *Nat. Phys.* **7**, 958 (2011).
9. L. Britnell *et al.*, *Science* **335**, 947 (2012).
10. T. Georgiou *et al.*, *Nat. Nanotechnol.* **8**, 100 (2013).
11. R. V. Gorbachev *et al.*, *Nat. Phys.* **8**, 896 (2012).
12. C. R. Dean *et al.*, *Nat. Phys.* **7**, 693 (2011).
13. J. N. Coleman *et al.*, *Science* **331**, 568 (2011).
14. Q. H. Wang, K. Kalantar-Zadeh, A. Kis, J. N. Coleman, M. S. Strano, *Nat. Nanotechnol.* **7**, 699 (2012).
15. L. F. Mattheiss, *Phys. Rev. B* **8**, 3719 (1973).
16. A. Ayari, E. Cobas, O. Ogunladege, M. S. Fuhrer, *J. Appl. Phys.* **101**, 014507 (2007).
17. A. H. Castro Neto, *Phys. Rev. Lett.* **86**, 4382 (2001).
18. A. Kumar, P. K. Ahluwalia, *Eur. Phys. J. B* **85**, 186 (2012).
19. M. R. Hilton, P. D. Fleischauer, *Surf. Coat. Tech.* **54-55**, 435 (1992).
20. S. R. Cohen *et al.*, *Thin Solid Films* **324**, 190 (1998).
21. C. Ballif *et al.*, *Appl. Phys. A Mat. Sci. Process.* **62**, 543 (1996).
22. E. Fortin, W. M. Sears, *J. Phys. Chem. Solids* **43**, 881 (1982).
23. K. K. Kam, B. A. Parkinson, *J. Phys. Chem.* **86**, 463 (1982).
24. H. Tributsch, H. Gerischer, C. Clemens, E. Bucher, *Phys. Chem. Chem. Phys.* **83**, 655 (1979).
25. C. Lee, X. D. Wei, J. W. Kysar, J. Hone, *Science* **321**, 385 (2008).
26. A. Castellanos-Gomez *et al.*, *Nanoscale Res. Lett.* **7**, 233 (2012).
27. See supplementary materials on Science Online.
28. S. J. Haigh *et al.*, *Nat. Mater.* **11**, 764 (2012).
29. A. S. Mayorov *et al.*, *Nano Lett.* **11**, 2396 (2011).
30. A. H. Castro Neto, F. Guinea, N. M. R. Peres, K. S. Novoselov, A. K. Geim, *Rev. Mod. Phys.* **81**, 109 (2009).
31. B. E. A. Saleh, M. C. Teich, *Fundamentals of Photonics*. Wiley Series in Pure and Applied Optics (Wiley, New York, ed. 2, 2007).

32. V. V. Sobolev, V. V. Sobolev, *J. Appl. Spectrosc.* **61**, 532 (1994).
33. M. S. Dresselhaus *et al.*, *Acc. Chem. Res.* **35**, 1070 (2002).
34. B. Sachs *et al.*, Doping mechanisms in graphene-MoS₂ hybrids; arXiv:1304.2236 (2013).
35. M. Furchi *et al.*, *Nano Lett.* **12**, 2773 (2012).
36. P. Blake *et al.*, *Appl. Phys. Lett.* **91**, 063124 (2007).
37. R. V. Gorbachev *et al.*, *Small* **7**, 465 (2011).
38. S. M. Nie, S. R. Emory, *Science* **275**, 1102 (1997).
39. H. A. Atwater, A. Polman, *Nat. Mater.* **9**, 205 (2010).
40. T. J. Echtermeyer *et al.*, *Nature Communications* **2**, 458 (2011).
41. O. Hess *et al.*, *Nat. Mater.* **11**, 573 (2012).

Acknowledgments: This work was supported by the Royal Society, European Research Council, U.S. Army, EPSRC and European Science Foundation (ESF) under the EUROCORES Programme EuroGRAPHENE (GOSPEL). A.M. acknowledges support from the Swiss National Science Foundation. A.H.C.N. acknowledges support from the National Research Foundation (NRF) of Singapore through NRF-CRP award "Novel 2D materials with tailored properties: Beyond graphene" (R-144-000-295-281). Y.-J.K.'s work was supported by the Global Research Laboratory (GRL) Program (2011-0021972) of the Ministry of Education, Science and Technology, Korea. R.M.R. is thankful for the financial support of the Portuguese FCT under grant SFRH/BSAB/1249/2012.

Supplementary Materials

www.sciencemag.org/cgi/content/full/science.1235547/DC1
Materials and Methods
Supplementary Text
Figs. S1 to S9
References (42–50)

23 January 2013; accepted 18 April 2013
Published online 2 May 2013;
10.1126/science.1235547

Redox Heterogeneity in Mid-Ocean Ridge Basalts as a Function of Mantle Source

Elizabeth Cottrell^{1*} and Katherine A. Kelley²

The oxidation state of Earth's upper mantle both influences and records mantle evolution, but systematic fine-scale variations in upper mantle oxidation state have not previously been recognized in mantle-derived lavas from mid-ocean ridges. Through a global survey of mid-ocean ridge basalt glasses, we show that mantle oxidation state varies systematically as a function of mantle source composition. Negative correlations between Fe³⁺/ΣFe ratios and indices of mantle enrichment—such as ⁸⁷Sr/⁸⁶Sr, ²⁰⁸Pb/²⁰⁴Pb, Ba/La, and Nb/Zr ratios—reveal that enriched mantle is more reduced than depleted mantle. Because carbon may act to simultaneously reduce iron and generate melts that share geochemical traits with our reduced samples, we propose that carbon creates magmas at ridges that are reduced and enriched.

The composition and geophysical properties of Earth's mantle have evolved in response to oxygen fugacity (*f*O₂), a measure of the chemical potential of oxygen in solid systems (1, 2). Mantle-derived mid-ocean ridge basalts (MORBs) record *f*O₂ through the ratio of oxidized to total iron (Fe³⁺/ΣFe) (3),

and, because MORBs also record geochemically distinct mantle reservoirs, the potential exists to discover the existence and evolution of heterogeneities in the oxidation state of the mantle. Two previous large (*n* > 75) global surveys of Fe oxidation states in MORB pillow glass (4, 5) found no correlation between Fe³⁺/ΣFe ratios and mantle source composition, establishing the paradigm that oceanic upper mantle oxidation state is relatively uniform, buffered, and not linked to plate tectonic-scale processes. Other work (6) has proposed that enriched mantle domains may be more oxidized than normal MORB. We deter-

mined high-precision (±0.005) Fe³⁺/ΣFe ratios by micro-x-ray absorption near-edge structure (XANES) (7, 8) and trace element concentrations on 19 glasses (from seven geographical locations) that have not experienced substantial fractionation [i.e., primitive MORB with MgO > 8.5 weight % (wt %)] or plume influence (9) (table S1). Additionally, a partially overlapping set of 22 glasses (from 10 geographical locations) from ridge segments without plume influence, irrespective of MgO content, previously published Sr ± Pb ± Nd isotope ratios (table S1). The primitive data set spans 50% of the global range in Fe³⁺/ΣFe ratios, whereas the isotope data set spans the entire global range (fig. S1). Globally, the Fe³⁺/ΣFe ratio in MORB negatively correlates with MgO concentration, whereby the Fe³⁺/ΣFe ratio increases by ~0.03 as MgO decreases from 10 to 5 wt % (8) because Fe²⁺ preferentially partitions into fractionating mafic phases. In order to account for the effect of fractionation, the Fe³⁺/ΣFe ratios have been recalculated to an arbitrary reference value at MgO = 10 wt %, Fe³⁺/ΣFe₍₁₀₎, analogous to Fe₂O₃₍₈₎ in (4, 8). This correction is ~2% relative for the 19 primitive samples and is up to 11% (average of 7%) relative for the samples with isotopic data, but correlations between Fe³⁺/ΣFe ratios, trace elements, and isotopes are also evident in the uncorrected data (9) (fig. S1).

The glasses form subparallel arrays in ²⁰⁸Pb/²⁰⁴Pb-²⁰⁶Pb/²⁰⁴Pb space as a function of Fe³⁺/ΣFe ratio, with ²⁰⁸Pb/²⁰⁴Pb ratios increasing as

¹National Museum of Natural History, Smithsonian Institution, Washington, DC 20560, USA. ²Graduate School of Oceanography, University of Rhode Island, Narragansett, RI 02882, USA.

*Corresponding author. E-mail: cottrell@si.edu

a strong function of decreasing Fe oxidation state (Fig. 1, A and E). Reduced glasses also possess elevated $^{87}\text{Sr}/^{86}\text{Sr}$ ratios and tend to have lower $^{143}\text{Nd}/^{144}\text{Nd}$ ratios (Fig. 1, B and F). Oxygen fugacity, calculated from $\text{Fe}^{3+}/\Sigma\text{Fe}$ ratio and glass composition (10) and referenced to the quartz-fayalite-magnetite buffer (ΔQFM), also correlates with isotopic enrichment (Fig. 1, C and D).

These observations link the Fe oxidation state of erupted MORB to mantle source heterogeneity, with enriched samples more reduced than depleted ones, because no magmatic process can fractionate these isotopes. Moreover, because these signatures require ancient fractionation of radiogenic parent-daughter pairs, these data also require preservation of the factors that lead to

heterogeneity in $\text{Fe}^{3+}/\Sigma\text{Fe}$ ratio on plate tectonic time scales. For the primitive samples, $\text{Fe}^{3+}/\Sigma\text{Fe}_{(10)}$ ratios correlate strongly with enrichment in highly incompatible elements (e.g., Ba, Th, and Nb) (Fig. 2) such that the most enriched samples are also the most reduced. Moderate correlations are also evident between $\text{Fe}^{3+}/\Sigma\text{Fe}_{(10)}$ ratio and depletion of the high field strength elements Hf and Zr (Fig. 2, E and F). We define a Hf anomaly, Hf/Hf^* , relative to elements with similar compatibility during mantle melting, such as Sm and Nd [$\text{Hf}/\text{Hf}^* = \text{Hf}_N/\sqrt{(\text{Sm}_N \times \text{Nd}_N)}$], and observe that reduced samples also tend to have more negative Hf anomalies (fig. S3). By contrast, oxidation state does not correlate with ratios of mid to heavy rare earth elements such as Sm/Yb or Dy/Yb; the heavy rare earth element patterns in these samples are flat (fig. S4).

These data require a process that links source enrichment to a reduced oxidation state. This is contrary to the relationship expected if redox heterogeneities simply reflect a difference in the solid/liquid partition coefficient (D) between the two Fe species (i.e., $D^{\text{Fe}^{3+}} < D^{\text{Fe}^{2+}}$) (4, 5) or if enriched MORB derived from graphite-buffered melting at greater depth (6, 11), both of which would predict MORB enriched in incompatible elements to be more oxidized. Garnet-bearing lithologies previously implicated in the generation of enriched MORB [e.g., (12)] might hold back Fe^{3+} during melting; however, a silicate melt of a garnet-bearing source is inconsistent with the trace and major element characteristics of our reduced samples (supplementary text and figs. S4 and S5). Here, we hypothesize that control over the Fe oxidation state of MORB is exercised by another incompatible element: carbon.

Carbon concentration has the potential to control the eruptive $\text{Fe}^{3+}/\Sigma\text{Fe}$ ratios of MORBs such that the most-reduced basalts derive from sources with greater carbon concentrations (13). This is because reduced carbon, stabilized at depth by lower f_{O_2} (2), must fully oxidize upon ascent to be consistent with the oxidation state of the erupted basalts (8). Ferric iron becomes reduced in proportion to the initial carbon content (13, 14). To generate the observed range of $\text{Fe}^{3+}/\Sigma\text{Fe}$ ratios in either the primitive or isotope data sets solely through reduction of Fe_2O_3 by carbon requires variations in mantle C on the order of 80 to 170 parts per million (ppm). Independent estimates of mantle C concentration, which covary with enrichment (15), range from ~16 (depleted mantle) to >300 (enriched mantle) ppm (16). Thus, carbon may exert a primary influence on MORB oxidation state even if the erupted melts are too oxidized to be in equilibrium with graphite (8).

We cannot directly assess whether carbon concentration and oxidation state are correlated in our samples because CO_2 is partially degassed from most, if not all, MORB (17). Mantle carbon is constrained in two locations, however, and we note that trace element and carbon-enriched sample $2\pi\text{D}43$ (popping rock) suggests a mantle

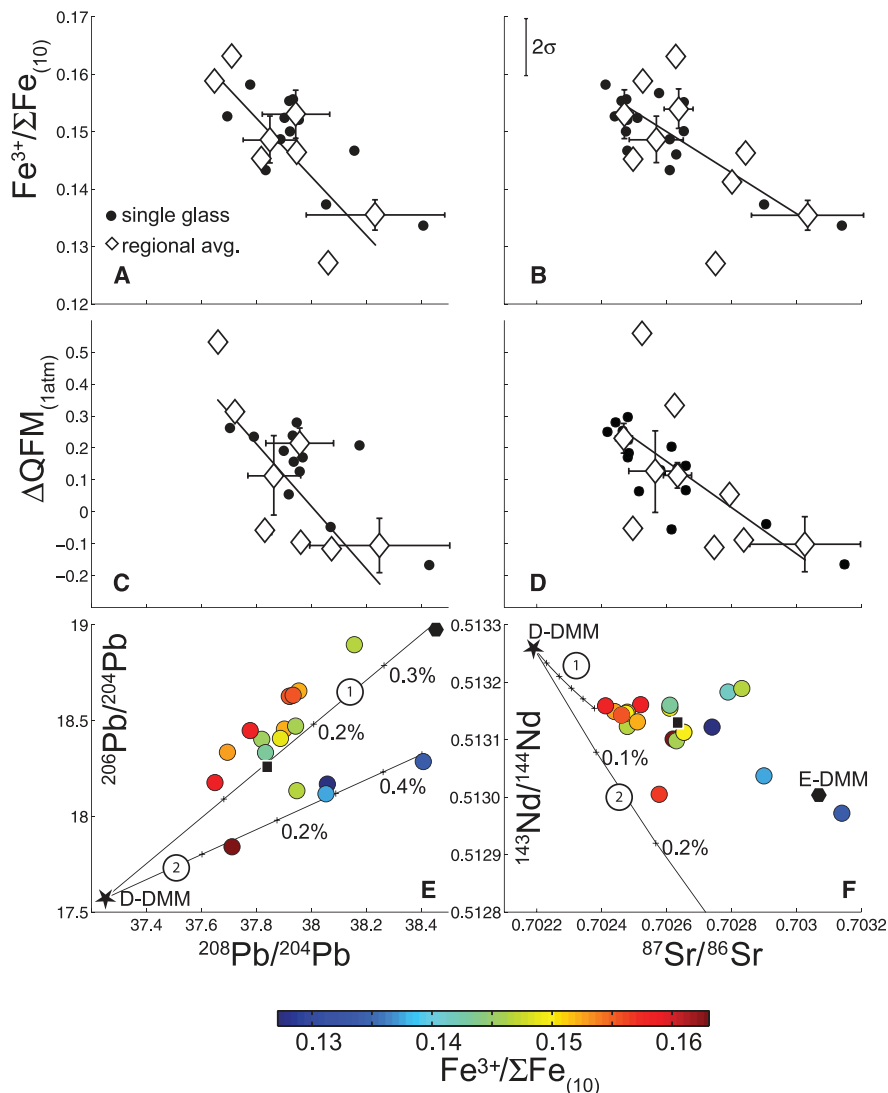


Fig. 1. Decrease in $\text{Fe}^{3+}/\Sigma\text{Fe}_{(10)}$ ratios as a function of isotopic enrichment. MORB $^{208}\text{Pb}/^{204}\text{Pb}$ and $^{87}\text{Sr}/^{86}\text{Sr}$ ratios versus $\text{Fe}^{3+}/\Sigma\text{Fe}_{(10)}$ ratios (A and B) and f_{O_2} relative to the QFM buffer at 1 atm (C and D). $\text{Fe}^{3+}/\Sigma\text{Fe}_{(10)}$ ratio accounts for 50 and 44% of the variance in these isotopic ratios, which is statistically significant at $P \leq 0.001$ (F -test results, table S3). Solid circles show individual analyses, and open diamonds show the regional averages and $\pm 1\sigma$ variability for each geographic location. MORB $^{208}\text{Pb}/^{204}\text{Pb}$ versus $^{206}\text{Pb}/^{204}\text{Pb}$ ratios (E) and $^{87}\text{Sr}/^{86}\text{Sr}$ versus $^{143}\text{Nd}/^{144}\text{Nd}$ ratios (F) as a function of $\text{Fe}^{3+}/\Sigma\text{Fe}_{(10)}$ ratios, showing a decrease in the oxidation state of Fe in the glasses as a function of isotopic enrichment. Color bar shows the relative Fe oxidation state of each sample. Curve 1 models 0.1% additions of a low-degree carbonatitic melt of subducted material to depleted-depleted MORB mantle (D-DMM; star), generated 2 Ga after subduction. Depleted (square) and enriched (hexagon) MORB mantle are from (20). Curve 2 demarcates additions of a low-degree carbonatitic melt of the same subducted source material as 1 but with the carbonatitic melt generated immediately after subduction at 2.8 Ga. The difference between these two curves is timing of the parent-daughter fractionation introduced by carbonatitic melting, where curve 1 assumes no fractionation of the subducted material until melting beneath the mid-ocean ridge and curve two assumes carbonatitic melt-induced fractionation immediately after subduction. Errors in isotopic ratios are as provided by the authors of those studies (9).

source with ~159 ppm CO₂ (18) and is more than two standard deviations more reduced than the global mean, whereas the trace element–depleted Siqueiros fracture zone basalts indicate ~72 ppm CO₂ in the source (19) and are among the most oxidized in our suite (Fig. 2 and fig. S1). Critically, some of the geochemical signatures most highly correlated with oxidation state [e.g., isotopes tending toward the EM-1 (enriched mantle) end member (20); elevated Ba/La, Th/La, Nd/Hf, Ba/Rb, Nb/Ta, and Nb/La ratios; and negative Hf anomalies] are not easily generated by silicate melting but are a natural consequence of melting in the presence of carbon (supple-

mentary text and fig. S3). Low-degree carbonatitic or kimberlitic melts may extract the highly incompatible elements to the melt phase while leaving Hf and Zr in the residue (21–23). Carbonatitic melts also fractionate radiogenic parent-daughter pairs, such that carbonatitic melts evolve more-radiogenic Sr and Pb and less-radiogenic Nd isotopic ratios over time, toward the EM-1 mantle component (22). Our samples are geographically distributed (fig. S2) and are not genetically related. Thus, it is not sensible to develop a petrogenetic model that accounts for each sample’s full major, trace, and radiogenic element signature. However, we do

show in Figs. 1 and 2 that addition of a few tenths of a percent of low-degree carbonatitic melt of subducted material to depleted silicate melt generates trace element and isotopic arrays that reproduce the most salient geochemical signatures associated with low Fe³⁺/ΣFe ratios (supplementary text).

The deep Earth is a large reservoir for carbon, continually replenished by subduction (24, 25), and thus the mixtures of low-degree carbonatitic and/or kimberlitic melts and high-degree silicate melts may be widespread depending on the distribution of carbon in the deep Earth (13, 23, 26). Before 2.3 billion years ago (Ga), anoxic conditions at Earth’s surface (27) would have resulted in subduction of reduced carbon associated with trace- and isotopically enriched sediment and crust into mantle that was already relatively oxidized (28). Subduction at 2.8 Ga may have created reduced domains in the mantle while enabling carbonate-fluxed melting to fractionate parent-daughter pairs consistent with those observed (Fig. 1). Today, the mantle’s descending *f*_{O₂} gradient should immobilize carbon through redox freezing (29); however, the potential of subducted carbonate to generate mobile reduced carbon species (2) cannot be ruled out. Any mobilization of reduced carbon may, upon decompression, result in melts that are simultaneously enriched and reduced (supplementary text and fig. S6). Additional mechanisms may exist to create geochemically enriched reducing domains in the mantle (30), but their geochemical implications for MORB are still unknown.

Our observations have important implications for the persistence of heterogeneities in mantle oxidation state through time. Far from being homogeneous or well-buffered, the mantle appears capable of retaining oxidation state information over plate tectonic time scales. This implies that redox-active elements such as H, C, S, and Fe do not buffer the upper mantle at uniform *f*_{O₂}. Rather, the Fe³⁺/ΣFe ratios of MORBs, like arcs (31), reflect variations in their sources.

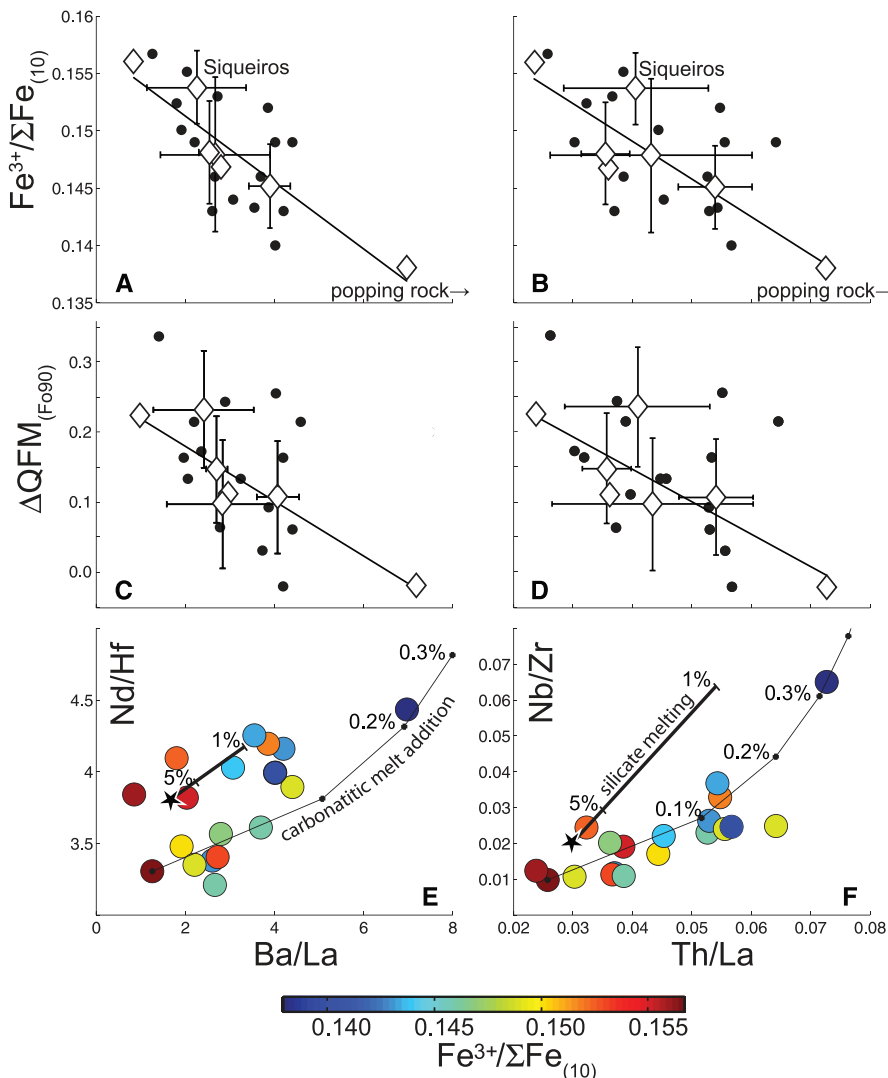


Fig. 2. Decrease in Fe³⁺/ΣFe₍₁₀₎ ratios with trace element enrichment in primitive glasses with >8.5 wt % MgO. (A and B) Ba/La and Th/La ratios decreasing as a function of Fe³⁺/ΣFe₍₁₀₎ ratio and the *f*_{O₂} of the source mantle at the average pressure and temperature of melt segregation (~0.7 to 1.3 GPa) relative to the QFM buffer (β) (C and D). Fe³⁺/ΣFe₍₁₀₎ ratio accounts for 53 and 43% of the variance in these trace element ratios, statistically significant at *P* ≤ 0.002 (*F*-test results, table S3). Solid circles show individual analyses, and open diamonds show the regional averages and ±1σ variability for each geographic location (popping rock Ba/La = 13.2, Th/La = 0.11, Fe³⁺/ΣFe₍₁₀₎ = 0.137). (E and F) Covariation of Ba/La with Nd/Hf ratios and Th/La with Nb/Zr ratios as a function of Fe³⁺/ΣFe₍₁₀₎ ratio. Lines model 0.1% additions (+) of a low-degree carbonatitic melt of subducted material to depleted sample VG5211 from Siqueiros (supplementary text). D-DMM (star) shown with silicate melt trajectory to 1% melt fraction. Errors in trace element ratios are smaller than the symbol sizes.

References and Notes

1. B. R. Frost, Ed., *Introduction to Oxygen Fugacity and Its Petrologic Importance* (BookCrafters, Chelsea, MI, 1991), vol. 25, pp. 1–9.
2. D. J. Frost, C. A. McCammon, *Annu. Rev. Earth Planet. Sci.* **36**, 389 (2008).
3. I. S. E. Carmichael, *Contrib. Mineral. Petrol.* **106**, 129 (1991).
4. A. Bézos, E. Humler, *Geochim. Cosmochim. Acta* **69**, 711 (2005).
5. D. M. Christie, I. S. E. Carmichael, C. H. Langmuir, *Earth Planet. Sci. Lett.* **79**, 397 (1986).
6. C. Ballhaus, *Contrib. Mineral. Petrol.* **114**, 331 (1993).
7. E. Cottrell, K. A. Kelley, A. Lanzirotti, R. A. Fischer, *Chem. Geol.* **268**, 167 (2009).
8. E. Cottrell, K. A. Kelley, *Earth Planet. Sci. Lett.* **305**, 270 (2011).
9. Materials and methods are available as supplementary materials on Science Online.
10. V. C. Kress, I. S. E. Carmichael, *Contrib. Mineral. Petrol.* **108**, 82 (1991).
11. J. D. Blundy, J. P. Brodholt, B. J. Wood, *Nature* **349**, 321 (1991).

12. Y. L. Niu, K. D. Collerson, R. Batiza, J. I. Wendt, M. Regelous, *J. Geophys. Res. Solid Earth* **104**, 7067 (1999).
13. V. Stagno, D. O. Ojwang, C. A. McCammon, D. J. Frost, *Nature* **493**, 84 (2013).
14. V. Stagno, D. J. Frost, *Earth Planet. Sci. Lett.* **300**, 72 (2010).
15. J. G. Moore, *Nature* **282**, 250 (1979).
16. R. Dasgupta, M. M. Hirschmann, *Earth Planet. Sci. Lett.* **298**, 1 (2010).
17. J. E. Dixon, E. Stolper, J. R. Delaney, *Earth Planet. Sci. Lett.* **90**, 87 (1988).
18. P. Cartigny, F. Pineau, C. Aubaud, M. Javoy, *Earth Planet. Sci. Lett.* **265**, 672 (2008).
19. A. E. Saal, E. H. Hauri, C. H. Langmuir, M. R. Perfit, *Nature* **419**, 451 (2002).
20. R. K. Workman, S. R. Hart, *Earth Planet. Sci. Lett.* **231**, 53 (2005).
21. R. Dasgupta, M. M. Hirschmann, *Nature* **440**, 659 (2006).
22. R. Dasgupta, M. M. Hirschmann, W. F. McDonough, M. Spiegelman, A. C. Withers, *Chem. Geol.* **262**, 57 (2009).
23. A. V. Girsnis, V. K. Bulatov, G. P. Brey, A. Gerdes, H. E. Höfer, *Lithos* **160-161**, 183 (2013).
24. R. Dasgupta, M. M. Hirschmann, A. C. Withers, *Earth Planet. Sci. Lett.* **227**, 73 (2004).
25. N. H. Sleep, K. Zahnle, *J. Geophys. Res. Planets* **106**, 1373 (2001).
26. R. Dasgupta *et al.*, *Nature* **493**, 211 (2013).
27. J. F. Kasting, D. H. Egler, S. P. Raeburn, *J. Geol.* **101**, 245 (1993).
28. D. Canil, *Nature* **389**, 842 (1997).
29. A. Rohrbach, M. W. Schmidt, *Nature* **472**, 209 (2011).
30. E. Bali, A. Audétat, H. Keppler, *Nature* **495**, 220 (2013).
31. K. A. Kelley, E. Cottrell, *Science* **325**, 605 (2009).

Acknowledgments: Data described in this paper are presented in the supplementary materials and are archived in the

PetDB database (www.earthchem.org/petdb). We thank F. Davis for discussion and are grateful for support from the Deep Carbon Observatory and NSF awards EAR-0841006 (E.C.) and EAR-0841108 (K.A.K.). Use of the National Synchrotron Light Source was supported by U.S. Department of Energy under contracts DE-AC02-98CH10886 and DE-FG02-92ER14244.

Supplementary Materials

www.sciencemag.org/cgi/content/full/science.1233299/DC1
Materials and Methods
Supplementary Text
Figs. S1 to S6
Tables S1 to S3
References (32–66)

28 November 2012; accepted 19 April 2013

Published online 2 May 2013;

10.1126/science.1233299

Hydrogen Isotopes in Lunar Volcanic Glasses and Melt Inclusions Reveal a Carbonaceous Chondrite Heritage

Alberto E. Saal,^{1*} Erik H. Hauri,² James A. Van Orman,³ Malcolm J. Rutherford¹

Water is perhaps the most important molecule in the solar system, and determining its origin and distribution in planetary interiors has important implications for understanding the evolution of planetary bodies. Here we report in situ measurements of the isotopic composition of hydrogen dissolved in primitive volcanic glass and olivine-hosted melt inclusions recovered from the Moon by the Apollo 15 and 17 missions. After consideration of cosmic-ray spallation and degassing processes, our results demonstrate that lunar magmatic water has an isotopic composition that is indistinguishable from that of the bulk water in carbonaceous chondrites and similar to that of terrestrial water, implying a common origin for the water contained in the interiors of Earth and the Moon.

During the solar system's early stages, the solar nebula was cold enough to allow the condensation of water into ice only beyond a distance of ~1 to 5 astronomical units (AU), termed the snowline (where 1 AU is the Earth-Sun distance). Planetesimals accreted beyond this distance grew into water-rich bodies, whereas those accreted closer to the Sun were devoid of water, resulting in relatively H₂O-depleted terrestrial planets and H₂O-enriched giant planets (1). Dynamical models suggest that water and other volatiles in the terrestrial planets have been the result of the accretion of volatile-rich asteroids coming from two different source regions at two distinct times: one from inside the Jupiter-formation region and the other between and beyond the giant planets, 5 to 100 million years (My) and >300 to 500 My after the formation of the first solids, respectively (1, 2).

Hydrogen isotopes (deuterium, D; and hydrogen, H) provide unique insight into the origin of water in planetary bodies (3–7). The solar sys-

tem consists of reservoirs containing water with an extremely wide range of D/H ratios (8). The variation in D/H ratios partly reflects the primordial gradient of water and other volatiles through the solar system as a function of distance from the

Sun (Fig. 1). Deuterium depletion is characteristic of the protosolar nebula (7), whereas the water ice from the outer solar system, such as in the Oort cloud comets, is enriched in D/H ratios by a factor of 2 or more over terrestrial water (3–7). The bulk water in carbonaceous chondrite meteorites (3) has a D/H ratio similar to that of Earth's water (9), suggesting that these meteorites might be responsible for bringing water to the terrestrial planets. However, a terrestrial-like D/H ratio has recently been measured on a Jupiter-Family comet (JFC), raising the possibility that Earth's water could have originated from cometary material (10). The similar D/H ratios among CI-CM carbonaceous chondrite meteorites, JFCs, and Earth may support the hypothesis of a common source region for the water of these celestial objects (3, 10, 11).

The Moon is thought to have formed in a giant collision between a planet and an early formed proto-Earth (12, 13). Although it has long been considered that this event removed essentially all hydrogen from the Moon (14), recent measurements on lunar volcanic glasses, melt inclusions, lunar apatites [Ca₅(PO₄)₃(F,Cl,OH)], and

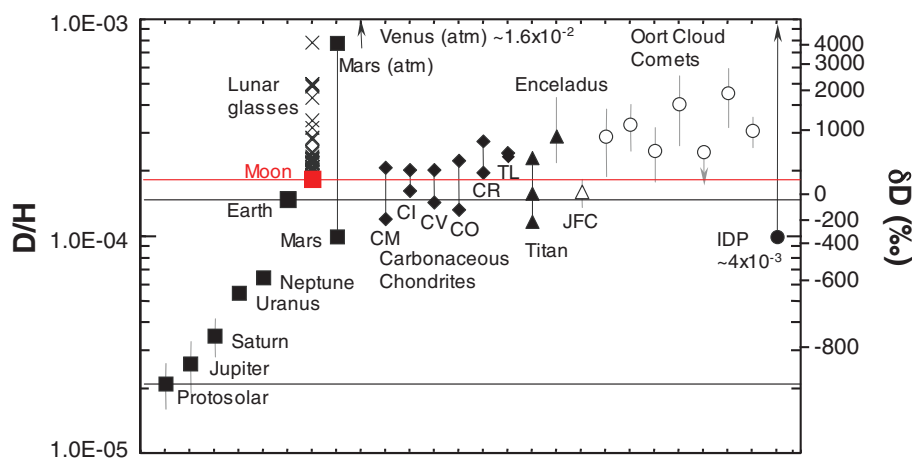


Fig. 1. The range of hydrogen isotopic composition in solar system objects. X symbols are the δD values of individual glass beads and melt inclusions corrected for cosmogenic contributions of H and D (see table S1). The glasses with errors $\pm 1000\%$ after spallation correction were not considered. The value for the lunar mantle (red square) represents the lowest δD and the highest water content measured in lunar melt inclusions. IDP, interplanetary dust particles; JFC, Jupiter-family comet. See (21) for references.

¹Department of Geological Sciences, Brown University, Providence, RI 02912, USA. ²Department of Terrestrial Magnetism, Carnegie Institution of Washington, Washington DC 20015, USA. ³Department of Geological Sciences, Case Western Reserve University, Cleveland, OH 44106, USA.

*Corresponding author. E-mail: asaal@brown.edu